communications physics

ARTICLE

https://doi.org/10.1038/s42005-023-01154-8 OPEN

Nematic fluctuations in an orbital selective superconductor $Fe_{1+y}Te_{1-x}Se_x$

Qianni Jiang[1], Yue Shi[2], Morten H. Christensen[3], Joshua J. Sanchez[1], Bevin Huang[1], Zhong Lin[1], Zhaoyu Liu[1], Paul Malinowski[1], Xiaodong Xu[1,2], Rafael M. Fernandes[3] & Jiun-Haw Chu[1✉]

$Fe_{1+y}Te_{1-x}Se_x$ is characterized by its complex magnetic phase diagram and highly orbital-dependent band renormalization. Despite this, the behavior of nematicity and nematic fluctuations, especially for high tellurium concentrations, remains largely unknown. Here we present a study of both B_{1g} and B_{2g} nematic fluctuations in $Fe_{1+y}Te_{1-x}Se_x$ ($0 \leq x \leq 0.53$) using the technique of elastoresistivity measurement. We discovered that the nematic fluctuations in two symmetry channels are closely linked to the corresponding spin fluctuations, confirming the intertwined nature of these two degrees of freedom. We also revealed an unusual temperature dependence of the nematic susceptibility, which we attributed to a loss of coherence of the d_{xy} orbital. Our results highlight the importance of orbital differentiation on the nematic properties of iron-based materials.

[1] Department of Physics, University of Washington, Seattle, WA 98195, USA. [2] Department of Material Science and Engineering, University of Washington, Seattle, WA 98195, USA. [3] School of Physics and Astronomy, University of Minnesota, Minneapolis, MN 55455, USA. ✉email: jhchu@uw.edu

The intricate interplay between magnetism and nematicity in different families of iron-based superconductors has attracted great interest in the past few years[1–4]. In iron pnictides, magnetism, and nematicity are tightly coupled; the antiferromagnetic (AFM) transition is always coincidental with, or closely preceded by, a tetragonal-to-orthorhombic structural transition. The proximity of the two transitions can be naturally explained within the spin-nematic scenario, where the structural transition is driven by a vestigial nematic order arising from fluctuations associated with the antiferromagnetic stripe transition (see Fig. 1a)[5–7]. In iron chalcogenides, the coupling between magnetism and nematicity is less obvious. FeSe undergoes a nematic phase transition without any long-range magnetic order[8,9], which has been interpreted as evidence that the nematic order in FeSe is of orbital origin[10]. Nevertheless, spin stripe fluctuations do develop below the nematic transition[10,11], and static stripe order can be induced by hydrostatic pressure[12,13].

While there are ongoing debates on the mechanism by which nematicity forms without static magnetism in FeSe[14–18], $Fe_{1+y}Te_{1-x}Se_x$ provides another platform to approach this problem. As selenium is replaced by tellurium (i.e., x is changed from 1 to 0), the nematic phase transition is suppressed and the superconducting critical temperature reaches optimal near the putative nematic quantum critical point ($x \sim 0.5$)[19,20]. In the high tellurium concentration regime ($x < 0.5$), inelastic neutron scattering experiments revealed a complex evolution of the spin correlations associated with different magnetic patterns[21–24]. Close to optimal doping, the wave-vector of spin fluctuations at low temperatures is (π, π) [in the crystallographic Brillouin zone], identical to the AFM order in the iron pnictides. As the tellurium concentration increases, both superconductivity and the (π, π) spin fluctuations disappear. The latter are replaced by short-range magnetic correlations with checkerboard character near $(0, \pi)$, and eventually at low temperatures the competing double-stripe phase forms in $Fe_{1+y}Te$ (Fig. 1b) by virtue of the ferro-orbital ordering that leads to the formation of ferromagnetic Zigzag chain[25–27]. Previous elastoresistivity measurements revealed a diverging B_{2g} nematic susceptibility in optimally doped $Fe_{1+y}Te_{1-x}Se_x$[20,28]. While the diverging nematic susceptibility is naturally expected as a consequence of the nematic quantum critical point, it is also consistent with the existence of (π, π) spin fluctuations found in the same doping. This finding suggests that nematic and magnetic fluctuations remain strongly intertwined even in the absence of static nematic and magnetic orders, consistent with previous inelastic neutron scattering study[23]. Nevertheless, in contrast to the magnetic sector, the behavior of nematic fluctuations for high tellurium concentrations (i.e., $x < 0.5$) is still poorly characterized. The compositional dependence of the nematic susceptibility in $Fe_{1+y}Te_{1-x}Se_x$ would therefore constitute an important step in the effort to elucidate the relationship between nematicity and magnetism.

Another motivation to study $Fe_{1+y}Te_{1-x}Se_x$ is to understand the influence of orbital selectivity on nematic instability. Orbital selectivity (or orbital differentiation) refers to the fact that different orbitals are renormalized differently by electronic correlations, a characteristic property of Hund's metals that appears to be much more prominent in the iron chalcogenides in comparison with the pnictides[29–31]. Experimentally, recent scanning tunneling microscopy (STM) measurements revealed the impact of orbital differentiation on the superconducting state[32]. Theoretically, it has been suggested that orbitally selective spin fluctuations may be the origin of nematicity without magnetism in FeSe[33]. The relation between orbital hybridization, spin fluctuations, and nematicity, was also suggested by an earlier inelastic neutron scattering experiment[23]. Nematic order was also proposed to enhance orbital selectivity by breaking the orbital degeneracy, leading to asymmetric effective masses in different d-orbitals[34]. The effect of orbital differentiation becomes even more extreme as selenium is replaced by tellurium. In $Fe_{1+y}Te_{1-x}Se_x$, angle-resolved photoemission spectroscopy

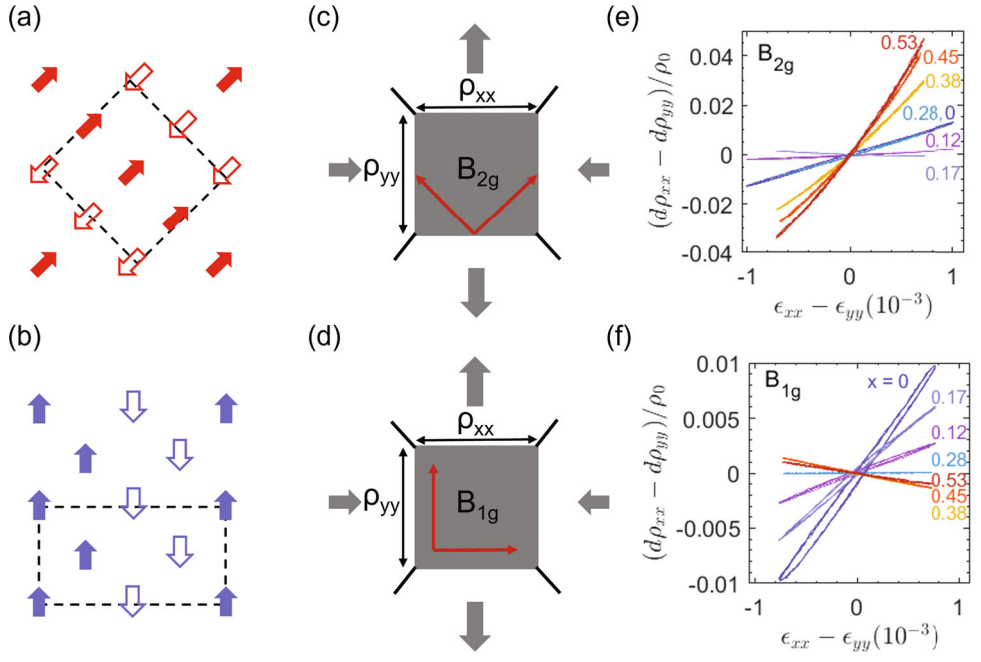

Fig. 1 Spin configurations and elastoresistivity configurations. a, **b** Schematic spin configurations of the (**a**) single-stripe phase, with $\mathbf{Q} = (\pi, \pi)$, and (**b**) double-stripe phase, with wave-vector $\mathbf{Q} = (\pi, 0)$. **c**, **d** Schematic diagrams of the Montgomery method for the elastoresistivity measurement in **c** B_{2g} and **d** B_{1g} configuration. **e**, **f** The anisotropic resistivity ($\rho_{xx}-\rho_{yy}$) as a function of anisotropic strain ($\epsilon_{xx}-\epsilon_{yy}$) for annealed $Fe_{1+y}Te_{1-x}Se_x$ ($0 \le x \le 0.53$) at $T = 20$ K in **e** B_{2g} and **f** B_{1g} channels. The B_{1g} elastoresistivity coefficient $m_{11}-m_{12}$ and B_{2g} elastoresistivity coefficient $2m_{66}$ can be obtained by fitting the linear slope of resistivity versus strain. The samples with high doping concentrations ($x = 0.38$, 0.45, 0.53) show predominantly a B_{2g} response while the low doping ones ($x = 0$, 0.12) show comparable B_{1g} and B_{2g} responses.

(ARPES) revealed a strong loss of spectral weight of the d_{xy} orbital at high temperatures, which was interpreted in terms of proximity to an orbital-selective Mott transition[35]. Similar drastic changes were also observed as a function of doping[36,37], mimicking the evolution of spin fluctuations. Nevertheless, the impact of orbital incoherence on nematicity remains little explored[38].

In this report, we present systematic measurements of both the B_{1g} and B_{2g} nematic susceptibilities of $Fe_{1+y}Te_{1-x}Se_x$ ($0 \le x \le 0.53$) using the elastoresistivity technique. We demonstrate that the doping dependence of the two nematic susceptibilities closely track the evolution of the corresponding spin fluctuations. In particular, a diverging B_{1g} nematic susceptibility is observed in the parent compound $Fe_{1+y}Te$, suggesting that the spin-nematic paradigm also applies to the double-stripe AFM order[39–41]. A diverging B_{2g} nematic susceptibility is observed over a wide range of doping ($0.17 \le x \le 0.53$), and its magnitude is strongly enhanced by both Se doping and annealing. In addition, the temperature dependence of the B_{2g} nematic susceptibility shows significant deviation from Curie–Weiss behavior above 50 K. This is in sharp contrast to the iron pnictides, where the Curie–Weiss temperature dependence extends all the way to 200 K. This unusual temperature dependence is captured by a theoretical calculation that includes the loss of spectral weight of the d_{xy} orbital, revealing its importance for B_{2g} nematic instability.

Results and discussion

Doping dependence and temperature dependence of elastoresistivity. By symmetry, the B_{1g} and B_{2g} nematic susceptibilities ($\chi_{B_{1g}}$ and $\chi_{B_{2g}}$) are proportional to the elastoresistivity coefficients $m_{11} - m_{12}$ and $2m_{66}$, respectively. We performed the elastoresistivity measurements in the Montgomery geometry, which enables simultaneous determination of the full resistivity tensor, hence the precise decomposition into different symmetry channels, as illustrated in Fig. 1c, d. Representative data of anisotropic resistivity as a function of anisotropic strain at 20 K in B_{2g} and B_{1g} channels are shown in Fig. 1e, f. The B_{1g} elastoresistivity coefficient $m_{11} - m_{12}$ and the B_{2g} one, $2m_{66}$, can be obtained by fitting the linear slope of resistivity versus strain. Samples with high doping concentrations ($x = 0.38, 0.45, 0.53$) show predominantly a B_{2g} response while the low doping ones ($x = 0, 0.12$) show comparable B_{1g} and B_{2g} responses.

Figure 2a, b shows the temperature dependence of $m_{11} - m_{12}$ and $2m_{66}$ of annealed $Fe_{1+y}Te_{1-x}Se_x$ for $0 \le x \le 0.53$. For $0.28 \le x \le 0.53$, $2m_{66}$ shows a strong temperature dependence that grows continuously as temperature decreases. For $x = 0.45$, $2m_{66}$ reaches a value of ~100, comparable to optimally doped pnictides. While preserving a similar diverging temperature dependence, the maximum value of $2m_{66}$ decreases rapidly as selenium concentration decreases, from 100 for $x = 0.45$ to 15 for $x = 0.28$. The magnitude of $2m_{66}$ continues to decrease but changes sign for $x = 0.17$. On the other hand, $m_{11} - m_{12}$ shows a diverging response when x is below 0.17, which is in the vicinity of the double-stripe AFM order. As selenium concentration increases, $m_{11} - m_{12}$ evolves to a temperature-independent response, with small kinks at low temperatures likely coming from contamination of $2m_{66}$ due to misalignment. Overall, our observation of the doping dependence of $2m_{66}$ and $m_{11} - m_{12}$ is consistent with the evolution of low-temperature spin fluctuations from predominantly $(\pi, 0)$ at small x to predominantly (π, π) at optimal doping $x \sim 0.5$[21–24].

To gain more insight, we fit the $2m_{66}$ and $m_{11} - m_{12}$ to a Curie–Weiss temperature dependence:

$$m = m^0 + \frac{\lambda}{a(T - T^*)} \quad (1)$$

For the parent compound $Fe_{1+y}Te$, $m_{11} - m_{12}$ can be well fitted to a Curie–Weiss behavior in the temperature range just above the double stripe AFM ordering temperature $T_{mag} = 71.5$ K (Fig. 2c). The fitted Curie–Weiss temperature T^* as listed in Supplementary Table III is slightly smaller than T_{mag}. Despite the smaller absolute value (~10 at maximum), the behavior of $m_{11} - m_{12}$ is reminiscent of the $2m_{66}$ in the parent phase of iron pnictides, suggesting that the spin-nematic mechanism is still at play here, in agreement with theoretical expectations[39–41].

Figure 2d shows the Curie–Weiss fitting of $2m_{66}$ for the $x = 0.45$ sample. The fitting of $2m_{66}$ only works at low temperatures, as can be seen in the linear temperature dependence of $|2m_{66} - 2m_{66}^0|^{-1}$ below 50K. It shows a significant deviation for temperature >50 K. The T^* obtained from the low-temperature fitting of $2m_{66}$ is close to 0K. Intriguingly, the T^* extracted from the Curie–Weiss fitting is approximately zero for all $0.17 \le x \le 0.53$, while the Curie constant λ/a decreases as x decreases (Supplementary Table II). While the number of doping concentrations studied in the current work is insufficient to

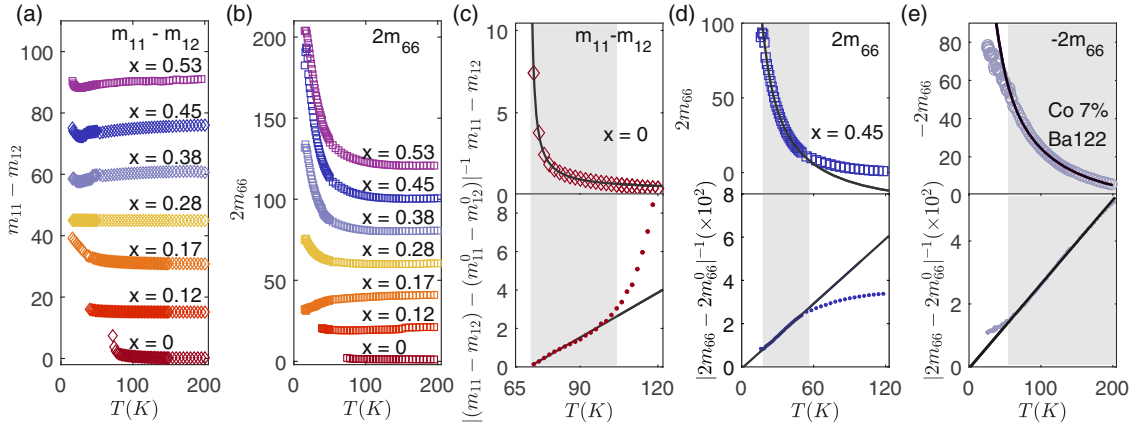

Fig. 2 Temperature and doping dependence of nematic fluctuations of annealed $Fe_{1+y}Te_{1-x}Se_x$. **a** Temperature and doping dependence of nematic fluctuations in the B_{1g} channel, with elastoresistivity coefficient $m_{11} - m_{12}$, and **b** B_{2g} channel, with $2m_{66}$. For clarity, the elastoresistivity data for each doping are offset by 15 and 20 in **a**, **b**, respectively. **c**–**e** Temperature dependence of **c** $m_{11} - m_{12}$ for $x = 0$, **d** $2m_{66}$ for $x = 0.45$ and **e** $-2m_{66}$ for $Ba(Fe_{0.93}Co_{0.07})_2As_2$. Lower panels show the inverse. Solid black curves are Curie–Weiss fits. The optimal fitting range is determined by the greatest corresponding adjusted R-square value (see Supplementary Note 4). Shaded gray regions indicate the range of temperatures where the elastoresistivity coefficients follow a Curie–Weiss law.

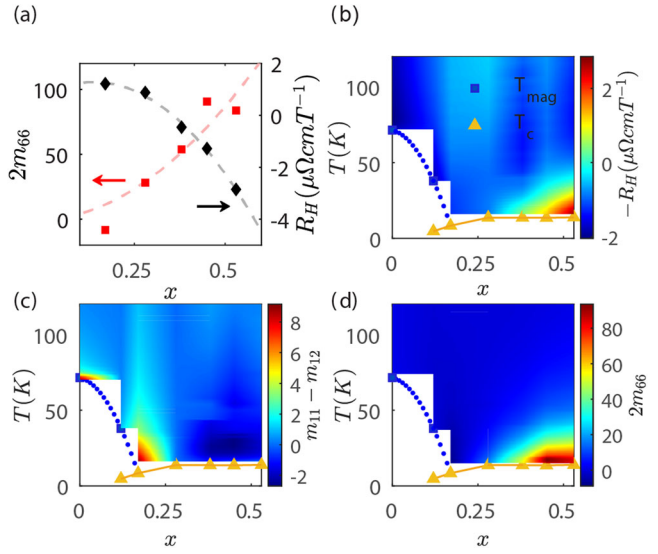

Fig. 3 Comparison between the elastoresistivity and the Hall coefficient R_H. **a** Doping dependence of the B_{2g} elastoresistivity coefficient $2m_{66}$ (red squares) and of R_H (black diamonds) at 16K. Dashed lines are guide to the eyes. **b** Colormap of the negative Hall coefficient $-R_H$ (raw data see Supplementary Note 5), **c** of $m_{11}-m_{12}$ **d** and of $2m_{66}$ as a function of temperature and doping. The double-spin stripe and the superconducting transition temperatures are denoted as blue squares and yellow triangles, respectively.

support a power law analysis, $2m_{66}$ at constant $T = 16$ K appears to be diverging as x increases from 0.17 to 0.45 (Fig. 3a). Both the doping dependence and the near zero T^* are consistent with the existence of a putative nematic quantum critical point at $x \sim 0.5$ discovered recently[20].

This deviation from Curie–Weiss at high temperatures is very unusual. In the iron pnicitides, such a deviation was only observed at low temperatures in transition-metal doped $BaFe_2As_2$ (Fig. 2e) and LaFeAsO[42]. This unusual temperature dependence of $2m_{66}$ is consistent with the thermal evolution of spin correlations observed by neutron scattering[43] and appears to echo the coherent-incoherent crossover observed by ARPES[35], where the spectral weight of the d_{xy} orbital is strongly suppressed as the temperature increases or as the selenium concentration decreases. To further confirm this correlation, we measured the Hall coefficient R_H, which has been demonstrated to be a good indicator of this incoherent-to-coherent crossover[36,44,45]. The recovery of the d_{xy} spectral weight is generally correlated with a sign-change of R_H[45] from positive to negative. Figure 3a shows the low-temperature R_H and $2m_{66}$ as a function of doping, whereas Fig. 3b–d contain the full temperature and doping dependence of R_H, $m_{11}-m_{12}$, and $2m_{66}$, respectively. These plots reveal the strong correlation between a negative R_H and an enhancement of $2m_{66}$.

Effect of annealing. The properties of $Fe_{1+y}Te_{1-x}Se_x$ also depend on the amount of excess iron, which can only be removed by annealing[46]. Taking $x = 0.45$ as an example, the resistance of the annealed sample is metallic for temperatures below 150 K (Fig. 4a). As Fig. 4b shows, at around 40 K the Hall coefficient of the annealed sample turns from positive to negative, which is a signature of incoherent to coherent crossover[36,44,45,47]. In contrast, the resistance of the as-grown sample shows a weakly insulating upturn at low temperatures (Fig. 4a black dashed curve), and the Hall coefficient remains positive at all temperatures (Fig. 4b black circles), indicating that the d_{xy} orbital is still

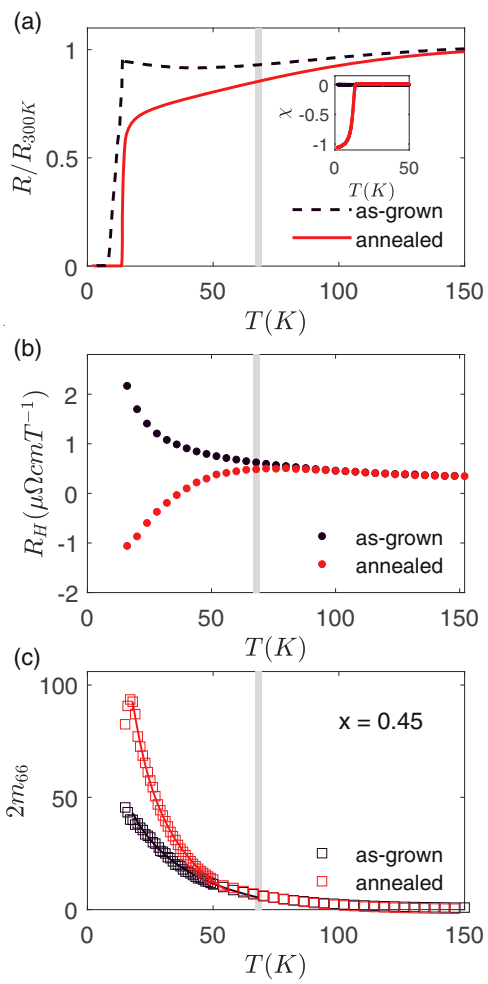

Fig. 4 The effect of annealing on the nematic susceptibility of $Fe_{1+y}Te_{1-x}Se_x$. **a**–**c** Temperature dependence of (**a**) normalized in-plane resistivity (R/R_{300K}), **b** Hall coefficient R_H and **c** elastoresistivity coefficient $2m_{66}$ of as-grown (black) and annealed (red) samples for $x = 0.45$. The vertical gray line marks the temperature below which the behavior of annealed and as-grown samples starts to deviate from each other. Inset of **a** shows the temperature dependence of the zero field cooling (ZFC) magnetic susceptibility measured at 100Oe (H||ab). The superconducting volume fraction is significantly enhanced for the annealed sample.

incoherent at low temperatures. Interestingly, at the same temperature where the resistance and the Hall coefficient of the as-grown and annealed samples depart from each other, the elastoresistivity coefficient $2m_{66}$ shows a pronounced enhancement for the annealed sample (Fig. 4c). Such an enhancement was observed in all annealed samples (Supplementary Note 2), providing further evidence of the correlation between the enhancement of the nematic susceptibility and the coherence of the d_{xy} orbital.

Effect of orbital selectivity on nematic fluctuations. The doping and annealing dependences of $2m_{66}$ presented above indicate that the B_{2g} nematic susceptibility also have an orbitally selective character. This is in agreement with a recent theoretical calculation that reveals a strongly orbitally dependent nematic susceptibility. In particular, the d_{xy} orbital contributes most to the overall nematic instability[48]. To gain more insight, we calculated the nematic susceptibility with and without a reduced spectral weight in the d_{xy} orbital to simulate the orbital correlation effect in

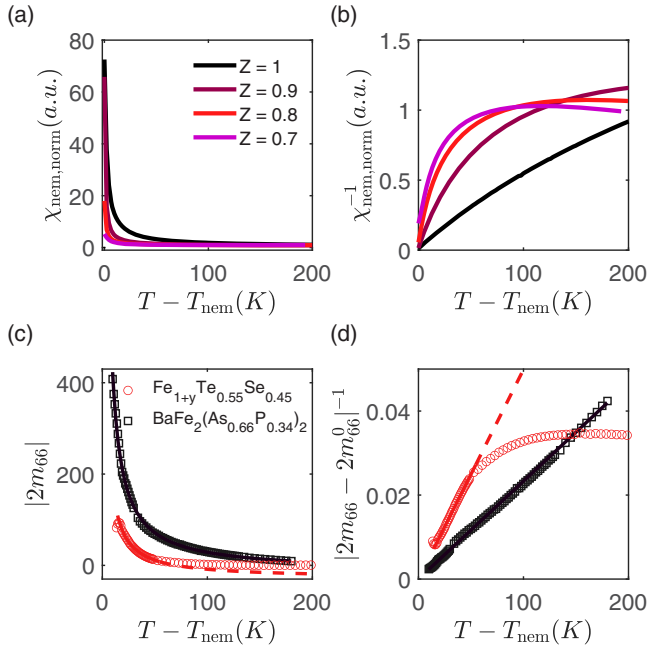

Fig. 5 Effect of orbital selectivity on nematic fluctuations. a, **b** Theoretical calculation of the normalized nematic susceptibility χ_{nem} (**a**) and its inverse (**b**), plotted as a function of the relative temperature with respect to the theoretical nematic transition temperature ($T - T_{\mathrm{nem}}$) for different spectral weight $0.7 \leq Z_{xy} \leq 1$. **c**, **d** Temperature dependence of **c** $|2m_{66}|$ and **d** $|2m_{66} - 2m^0_{66}|^{-1}$ of optimally doped $Fe_{1+y}Te_{0.55}Se_{0.45}$ (red circles) and $BaFe_2(As_{0.66}P_{0.34})_2$ (black squares). The red and black lines show Curie–Weiss fittings. The data for $BaFe_2(As_{0.66}P_{0.34})_2$ follows a Curie–Weiss behavior all the way up to 200K, whereas for $Fe_{1+y}Te_{0.55}Se_{0.45}$, it deviates from Curie–Weiss behavior above ~50 K.

$Fe_{1+y}Te_{1-x}Se_x$ and $BaFe_2(As_{1-x}P_x)_2$, respectively. The calculated B_{2g} nematic susceptibility and its inverse are plotted in Fig. 5a, b. The excellent agreement with the experimentally measured $2m_{66}$ and $|2m_{66} - 2m^0_{66}|^{-1}$ (Fig. 5c, d) confirms the orbitally selective nature of the nematic susceptibility.

Indeed, previous theoretical works have highlighted the impact of orbital degrees of freedom on spin-driven nematicity[17,33,34,49–51]. Using a slave-spin approach, ref. [38] found a suppression of the orbital-nematic susceptibility due to orbital incoherence. To model our data, we employ the generalized random phase approximation (RPA) of ref. [48] to compute the spin-driven nematic susceptibility for the five-orbital Hubbard-Kanamori model (details in Supplementary Note 6). For fully coherent orbitals, it was found that the largest contribution to the nematic susceptibility χ_{nem} comes from the d_{xy} orbital. Thus, one expects that χ_{nem} would be suppressed if the d_{xy} orbital were to become less coherent.

To verify this scenario, we calculated how χ_{nem} changes upon suppressing the spectral weight Z_{xy} of the d_{xy} orbital. For our purposes, the reduction in Z_{xy} acts phenomenologically as a proxy of the incoherence of this orbital, similarly to ref. [32], but its microscopic origin is not important. Fig. 5a, b contrasts the nematic susceptibility for $0.7 \leq Z_{xy} \leq 1$. We note two main trends arising from the suppression of d_{xy} spectral weight: first, as anticipated, the nematic susceptibility (and the underlying nematic transition temperature, which is non-zero in the model) is reduced (Fig. 5a). Second, its temperature dependence changes from a Curie–Weiss-like behavior over an extended temperature range to a behavior in which the inverse nematic susceptibility quickly saturates and strongly deviates from a linear-in-T dependence already quite close to the nematic transition (Fig. 5b). These behaviors are similar to those displayed by the elastoresistance data shown in Fig. 5c, d, with $Z_{xy} = 1$ mimicking the behavior of optimally P-doped $BaFe_2As_2$ and $Z_{xy} < 1$, of optimally doped $Fe_{1+y}Te_{1-x}Se_x$. Interestingly, the susceptibility associated with (π, π) fluctuations is also suppressed by the decrease in Z_{xy}, in qualitative agreement with the neutron scattering experiments[52] (for a more detailed discussion, see Supplementary Note 6). Of course, since Z_{xy} in our model is an input, and not calculated microscopically, our model is useful to capture tendencies, but not to extract the experimental value of Z_{xy}. Furthermore, note that in our calculation Z_{xy} is temperature-independent, while in the experiment it changes with temperature.

Conclusions

In summary, our results reveal the close connection between nematic fluctuations and spin fluctuations in $Fe_{1+y}Te_{1-x}Se_x$ for both B_{1g} and B_{2g} channels. Additionally, the unusual temperature dependence of the B_{2g} nematic susceptibility can be attributed to the coherent-to-incoherent crossover experienced by the d_{xy} orbital, providing direct evidence for the orbital selectivity of the nematic instability. Our work presents $Fe_{1+y}Te_{1-x}Se_x$ as an ideal platform to study the physics of intertwined orders in a strongly correlated Hund's metal.

Methods

Crystal growth. Single crystals of $Fe_{1+y}Te_{1-x}Se_x$ were grown by the modified Bridgeman method. The electrical, magnetic, and superconducting properties of $Fe_{1+y}Te_{1-x}Se_x$ are known to sensitively depend on y, the amount of excess iron. To study these effects, crystals were annealed in selenium vapor to reduce the amount of excess iron. Crystals are cleaved into thin slices (~1 mm), loaded in a crucible with another crucible of an appropriate amount (~the amount of excess iron in atomic weight) of selenium powder beneath it, sealed in quartz tubes, and annealed at 500 °C for a week.

Elastoresistivity measurements. The elastoresistivity measurements were performed in the Montgomery geometry, which enables simultaneous determination of the full resistivity tensor[28]. Crystals are prepared into thin square plates with edges along the Fe-Fe (B_{2g}) and Fe-Chalcogen (B_{1g}) bonding directions. The crystal orientation is determined by polarization-resolved Raman spectroscopy, as shown in Supplementary Note 1. Samples were glued on the sidewall of a piezoelectric stack, which generates a linear combination of anisotropic and isotropic strain. Electrical contacts made at the four corners enable the simultaneous determinations of the resistivities along two perpendicular directions of the same piece of sample. This setup allows the precise decomposition into the anisotropic resistivity change (B_{1g} and B_{2g}) $\Delta\rho_{xx} - \Delta\rho_{yy}$ and isotropic resistivity change (A_{1g}) $\Delta\rho_{xx} + \Delta\rho_{yy}$ in response to different symmetries of strain (see details in Supplementary Note 3).

Data availability

All data needed to evaluate the conclusions are present in the paper and supplementary materials. Additional data are available from the corresponding author on reasonable request.

Received: 6 June 2022; Accepted: 17 February 2023;
Published online: 01 March 2023

References

1. Fernandes, R. M., Chubukov, A. V. & Schmalian, J. What drives nematic order in iron-based superconductors? *Nat. Phys.* **10**, 97–104 (2014).
2. Dai, P. Antiferromagnetic order and spin dynamics in iron-based superconductors. *Rev. Mod. Phys.* **87**, 855–896 (2015).
3. Si, Q., Yu, R. & Abrahams, E. High-temperature superconductivity in iron pnictides and chalcogenides. *Nat. Rev. Mater.* **1**, 16017 (2016).
4. Fernandes, R. M. et al. Iron pnictides and chalcogenides: a new paradigm for superconductivity. *Nature* **601**, 35–44 (2022).
5. Fang, C., Yao, H., Tsai, W.-F., Hu, J. & Kivelson, S. A. Theory of electron nematic order in LaFeAsO. *Phys. Rev. B* **77**, 224509 (2008).
6. Xu, C., Müller, M. & Sachdev, S. Ising and spin orders in the iron-based superconductors. *Phys. Rev. B* **78**, 020501 (2008).

7. Fernandes, R. M., Chubukov, A. V., Knolle, J., Eremin, I. & Schmalian, J. Preemptive nematic order, pseudogap, and orbital order in the iron pnictides. *Phys. Rev. B* **85**, 024534 (2012).
8. McQueen, T. M. et al. Tetragonal-to-orthorhombic structural phase transition at 90K in the superconductor $Fe_{1.01}Se$. *Phys. Rev. Lett.* **103**, 057002 (2009).
9. Böhmer, A. E. & Kreisel, A. Nematicity, magnetism and superconductivity in FeSe. *J. Phys. Condens. Matter* **30**, 023001 (2017).
10. Baek, S.-H. et al. Orbital-driven nematicity in FeSe. *Nat. Mater.* **14**, 210–214 (2015).
11. Wang, Q. et al. Strong interplay between stripe spin fluctuations, nematicity and superconductivity in FeSe. *Nat. Mater.* **15**, 159–163 (2016).
12. Kothapalli, K. et al. Strong cooperative coupling of pressure-induced magnetic order and nematicity in FeSe. *Nat. Commun.* **7**, 1–6 (2016).
13. Matsuura, K. et al. Maximizing tc by tuning nematicity and magnetism in $FeSe_{1-x}S_x$ superconductors. *Nat. Commun.* **8**, 1143 (2017).
14. Glasbrenner, J. K. et al. Effect of magnetic frustration on nematicity and superconductivity in iron chalcogenides. *Nat. Phys.* **11**, 953–958 (2015).
15. Wang, F., Kivelson, S. A. & Lee, D.-H. Nematicity and quantum paramagnetism in FeSe. *Nat. Phys.* **11**, 959–963 (2015).
16. Yu, R. & Si, Q. Antiferroquadrupolar and ising-nematic orders of a frustrated bilinear-biquadratic heisenberg model and implications for the magnetism of FeSe. *Phys. Rev. Lett.* **115**, 116401 (2015).
17. Chubukov, A. V., Khodas, M. & Fernandes, R. M. Magnetism, superconductivity, and spontaneous orbital order in iron-based superconductors: which comes first and why? *Phys. Rev. X* **6**, 041045 (2016).
18. Yamakawa, Y. & Kontani, H. Nematicity, magnetism, and superconductivity in FeSe under pressure: unified explanation based on the self-consistent vertex correction theory. *Phys. Rev. B* **96**, 144509 (2017).
19. Terao, K., Kashiwagi, T., Shizu, T., Klemm, R. A. & Kadowaki, K. Superconducting and tetragonal-to-orthorhombic transitions in single crystals of $FeSe_{1-x}Te_x$($0 \le x \le 0.61$). *Phys. Rev. B* **100**, 224516 (2019).
20. Ishida, K. et al. Pure nematic quantum critical point accompanied by a superconducting dome. *Proc. Natl Acad. Sci.* **119**, e2110501119 (2022).
21. Lumsden, M. D. et al. Evolution of spin excitations into the superconducting state in $FeTe_{1-x}Se_x$. *Nat. Phys.* **6**, 182–186 (2010).
22. Liu, T. J. et al. From (π,0) magnetic order to superconductivity with (π,π) magnetic resonance in $Fe_{1.02}Te_{1-x}Se_x$. *Nat. Mater.* **9**, 718–720 (2010).
23. Zaliznyak, I. et al. Spin-liquid polymorphism in a correlated electron system on the threshold of superconductivity. *Proc. Natl. Acad. Sci.* **112**, 10316–10320 (2015).
24. Xu, Z. et al. Coexistence of superconductivity and short-range double-stripe spin correlations in te-vapor annealed $FeTe_{1-x}Se_x$ ($x \le 0.2$). *Phys. Rev. B* **97**, 214511 (2018).
25. Li, S. et al. First-order magnetic and structural phase transitions in $Fe_{1+y}Se_xTe_{1-x}$. *Phys. Rev. B* **79**, 054503 (2009).
26. Zaliznyak, I. A. et al. Unconventional temperature enhanced magnetism in $Fe_{1.1}Te$. *Phys. Rev. Lett.* **107**, 216403 (2011).
27. Fobes, D. et al. Ferro-orbital ordering transition in iron telluride $Fe_{1+y}Te$. *Phys. Rev. Lett.* **112**, 187202 (2014).
28. Kuo, H.-H., Chu, J.-H., Palmstrom, J. C., Kivelson, S. A. & Fisher, I. R. Ubiquitous signatures of nematic quantum criticality in optimally doped Fe-based superconductors. *Science* **352**, 958–962 (2016).
29. Yin, Z. P., Haule, K. & Kotliar, G. Kinetic frustration and the nature of the magnetic and paramagnetic states in iron pnictides and iron chalcogenides. *Nat. Mater.* **10**, 932–935 (2011).
30. Lanatà, N. et al. Orbital selectivity in hund's metals: the iron chalcogenides. *Phys. Rev. B* **87**, 045122 (2013).
31. de' Medici, L., Giovannetti, G. & Capone, M. Selective Mott physics as a key to iron superconductors. *Phys. Rev. Lett.* **112**, 177001 (2014).
32. Sprau, P. O. et al. Discovery of orbital-selective Cooper pairing in FeSe. *Science* **357**, 75–80 (2017).
33. Fanfarillo, L., Benfatto, L. & Valenzuela, B. Orbital mismatch boosting nematic instability in iron-based superconductors. *Phys. Rev. B* **97**, 121109 (2018).
34. Yu, R., Zhu, J.-X. & Si, Q. Orbital selectivity enhanced by nematic order in FeSe. *Phys. Rev. Lett.* **121**, 227003 (2018).
35. Yi, M. et al. Observation of universal strong orbital-dependent correlation effects in iron chalcogenides. *Nat. Commun.* **6**, 7777 (2015).
36. Liu, Z. K. et al. Experimental observation of incoherent-coherent crossover and orbital-dependent band renormalization in iron chalcogenide superconductors. *Phys. Rev. B* **92**, 235138 (2015).
37. Huang, J. et al. Correlation-driven electronic reconstruction in $FeTe_{1-x}Se_x$. *Commun. Phys.* **5**, 29 (2022).
38. Fanfarillo, L., Giovannetti, G., Capone, M. & Bascones, E. Nematicity at the hund's metal crossover in iron superconductors. *Phys. Rev. B* **95**, 144511 (2017).
39. Zhang, G., Glasbrenner, J. K., Flint, R., Mazin, I. I. & Fernandes, R. M. Double-stage nematic bond ordering above double stripe magnetism: application to $BaTi_2Sb_2O$. *Phys. Rev. B* **95**, 174402 (2017).
40. Bishop, C. B., Herbrych, J., Dagotto, E. & Moreo, A. Possible bicollinear nematic state with monoclinic lattice distortions in iron telluride compounds. *Phys. Rev. B* **96**, 035144 (2017).
41. Borisov, V., Fernandes, R. M. & Valentí, R. Evolution from B_{2g} nematics to B_{1g} nematics in heavily hole-doped iron-based superconductors. *Phys. Rev. Lett.* **123**, 146402 (2019).
42. Hong, X. et al. Evolution of the nematic susceptibility in $LaFe_{1-x}Co_xAsO$. *Phys. Rev. Lett.* **125**, 067001 (2020).
43. Xu, Z. et al. Thermal evolution of antiferromagnetic correlations and tetrahedral bond angles in superconducting $FeTe_{1-x}Se_x$. *Phys. Rev. B* **93**, 104517 (2016).
44. Ding, X., Pan, Y., Yang, H. & Wen, H.-H. Strong and nonmonotonic temperature dependence of Hall coefficient in superconducting $K_xFe_{2-y}Se_2$ single crystals. *Phys. Rev. B* **89**, 224515 (2014).
45. Otsuka, T. et al. Incoherent-coherent crossover and the pseudogap in Te-annealed superconducting $Fe_{1+y}Te_{1-x}Se_x$ revealed by magnetotransport measurements. *Phys. Rev. B* **99**, 184505 (2019).
46. Sun, Y., Shi, Z. & Tamegai, T. Review of annealing effects and superconductivity in $Fe_{1+y}Te_{1-x}Se_x$ superconductors. *Supercond. Sci. Technol.* **32**, 103001 (2019).
47. Li, Y. et al. Electronic properties of the bulk and surface states of $Fe_{1+y}Te_{1-x}Se_x$. *Nat. Mater.* **20**, 1221–1227 (2021).
48. Christensen, M. H., Kang, J., Andersen, B. M. & Fernandes, R. M. Spin-driven nematic instability of the multiorbital hubbard model: application to iron-based superconductors. *Phys. Rev. B* **93**, 085136 (2016).
49. Fanfarillo, L., Cortijo, A. & Valenzuela, B. Spin-orbital interplay and topology in the nematic phase of iron pnictides. *Phys. Rev. B* **91**, 214515 (2015).
50. Onari, S., Yamakawa, Y. & Kontani, H. Sign-reversing orbital polarization in the nematic phase of FeSe due to the C_2 symmetry breaking in the self-energy. *Phys. Rev. Lett.* **116**, 227001 (2016).
51. Xing, R.-Q., Classen, L. & Chubukov, A. V. Orbital order in FeSe: the case for vertex renormalization. *Phys. Rev. B* **98**, 041108 (2018).
52. Xu, Z. et al. Temperature-dependent transformation of the magnetic excitation spectrum on approaching superconductivity in $Fe_{1+y-x}(Ni/Cu)_xTe_{0.5}Se_{0.5}$. *Phys. Rev. Lett.* **109**, 227002 (2012).

Acknowledgements

We thank Ming Yi for the fruitful discussion. The work at UW was supported by NSF MRSEC at UW (DMR-1719797). The material synthesis was supported by the Northwest Institute for Materials Physics, Chemistry, and Technology (NW IMPACT) and the Gordon and Betty Moore Foundation's EPiQS Initiative, Grant GBMF6759 to J.-H.C. J.H.C. acknowledge the support of the David and Lucile Packard Foundation, the Alford P. Sloan Foundation and the State of Washington funded Clean Energy Institute. Theory work (M.H.C. and R.M.F.) was supported by the U.S. Department of Energy, Office of Science, Basic Energy Sciences, Materials Sciences, and Engineering Division, under Award No. DE-SC0020045. The Raman measurement is partially supported by the Department of Energy, Basic Energy Sciences, Materials Sciences and Engineering Division (DE-SC0012509).

Author contributions

J.-H.C. proposed and designed the research. J.-H.C., Q.J., and Y.S. carried out the elastoresistivity measurements with the help of Z.-Y.L. and P.M. The elastoresistivity data were analyzed by J.-H.C. and Q.J. Single crystals of $Fe_{1+y}Te_{1-x}Se_x$ were synthesized and annealed by Q.J., Y.S., and J.J.S. The polarized Raman spectroscopy was carried out by Q.J., B.H., Z.L., and X.X. Theoretical calculations were carried out by R.M.F. and M.H.C. Q.J. and J.-H.C. wrote the paper with input from all co-authors. J.-H.C. oversaw the project.

Competing interests

The authors declare no competing interests.

Additional information

Supplementary information The online version contains supplementary material available at https://doi.org/10.1038/s42005-023-01154-8.

Correspondence and requests for materials should be addressed to Jiun-Haw Chu.

Peer review information *Communications Physics* thanks Igor Zaliznyak, Federico Caglieris and the other, anonymous, reviewer(s) for their contribution to the peer review of this work.

Reprints and permission information is available at http://www.nature.com/reprints

Publisher's note Springer Nature remains neutral with regard to jurisdictional claims in published maps and institutional affiliations.